Effects of inflammation-induced oxidation on the dimerization of fibrinogen αC domain

Eric N. Pederson and Gianluca Interlandi*

Department of Bioengineering, University of Washington, Seattle, WA

98195, USA

Running title: *Oxidation of fibrinogen αC domain*

*Correspondence to: Gianluca Interlandi, Department of Bioengineering,

University of Washington Box 355061, 3720 15th Ave NE,

Seattle, WA 98195-5061, USA, Tel.: (206) 685-4435

Fax: (206) 685-3300, E-mail: gianluca@u.washington.edu

Abstract

Fibrinogen is a hemostatic plasma protein that can form protofibrils via 'knob-hole' interactions and then laterally aggregate into fibers. Inflammation-induced impairment of this process by oxidation of Met^{476} has been shown to produce dense clots that are resistant to fibrinolysis and pose the threat of thrombosis. To understand the structural basis for the mechanism, we performed enhanced sampling molecular dynamics simulations on the human αC domain dimer in implicit solvent. The only experimental structure for the αC domain is based on the bovine structure so the dimer was modeled using a human homology model. we selected the seven most sampled structures from the trajectories to understand how oxidation affects the stability of the dimer. Methionine oxidation increases flexibility of the αC domain, reduces the size of the hydrophobic core and inhibits dimerization. After evaluating the stability of the minima in explicit solvent, we calculated the interface occupancy of all residues and predicted 2 dimeric and 2 monomeric mutants. Met^{476}Gln and Leu^{478}Ala are expected to form monomers by disrupting their wild type contacts. In contrast, Thr^{486}Ala and Met^{476}Val are not expected to significantly change dimerization properties because Thr^{486}Ala displays no occupancy at the interface and Met^{476}Val is a functionally synonymous mutant.

1 Introduction

Fibrinogen is cleaved by thrombin to produce fibrin, which can stabilize platelets to form blood clots in the event of a vascular injury. These fibrin clots provide a barrier for pathogens, which prevents infection and improves healing outcomes. However, under inflammatory conditions, neutrophil lysozomal myeloperoxidase can convert H_2O_2, Cl^- and H_2O into HOCl, a powerful oxidant. HOCl can oxidize the C-terminal α chain Met^{476} into methionine sulfoxide ($Met(O)^{476}$) in a compact region known as the αC domain surrounded by intrinsically disordered region (Collet *et al.*, 2005; Medved, Gorkun, & Privalov, 1983; Shacter, Williams, Lim, & Levine, 1994; Weisel & Litivinov, 2013). The αC domain monomer is small and lacks a hydrophobic core. It consists of an N-terminal β-hairpin held together by a disulfide bond and a C-terminal pseudohairpin that lacks the characteristic hydrogen bonding (H-bond) along the backbone but adopts a similar conformation based on a bovine NMR solution structure as shown in Figure 1a (Burton, Tsurupa, Hantgan, Tjandra, & Medved, 2007; Burton, Tsurupa, Medved, & Tjandra, 2006). A human homology model as shown in Figure 1b, which shares 57% identity to the bovine sequence by BLAST (Madden, 2003). The NMR structure of the human sequence has not been resolved due to aggregation at high concentrations (Tsurupa *et al.*, 2009). Oxidized fibrin clots are denser, softer, and more resistant to fibrinolysis compared to normal clots. These oxidized clots pose the risk of embolus, which can be fatal (Weisel & Litivinov, 2013). Under acute inflammation, this mechanism may protect against pathogens with fibrinolytic activity (Esmon, Xu, & Lupu, 2011; Rosen *et al.*, 2009) but is potentially hazardous under chronic conditions such as diabetes mellitus (Lipinski, 2001; Martinez, Weisel, & Ischiropoulos, 2013; KM Weigandt *et al.*, 2012; White *et al.*, 2016). Traumatic injury is capable of inducing thrombosis and bleeding disorders and is associated with oxidized αC domain (White *et al.*, 2016). Patients with thrombotic diseases such as pulmonary embolism, stroke and heart attack tend to demonstrate pro-thrombotic fibrin clot structures made up of abnormally thin fibrin fibers with decreased clot porosity making them more likely to induce thrombosis (Davenport *et al.*, 2011; Esmon *et al.*, 2011; Martinez *et al.*, 2013; Weigandt *et al.*, 2012; KM Weigandt *et al.*, 2012; Weisel & Litivinov, 2013; Weisel & Medved, 2001; White *et al.*, 2016). In addition, hemorrhagic diseases such as hemophilia and trauma also display altered clot structure that contributes to bleeding morbidity and mortality (Davenport *et al.*, 2011; Leong *et al.*, 2017; Shacter *et al.*, 1994). This mechanism has not been elucidated at the structural level. Chicken fibrinogen αC domain does not homooligomerize to form fibers. Recombinant human fibrin containing a chicken αC domain displays clot morphologies that are notably similar to

oxidized fibrin clots (Ping *et al.*, 2011). This suggests that an impairment of αC domain interactions may be responsible for the adverse clot morphology.

Previous attempts to understand the structural mechanism of oligomerization have been inconclusive. Simulations of the oxidized αC monomer show an increased radius of gyration and more disorder, although it isn't clear how this affects oligomerization (Burney, White, & Pfaendtner, 2014). Previous predictions of αC domain oligomers have relied heavily on β-sheet interactions (Tsurupa *et al.*, 2015). We hypothesize that oxidation of Met^{476} affects homooligomer interactions, which can only be observed by simulating the dimer. To understand the energetics of αC domain folding upon oxidation, we constructed free energy landscapes (FELs) of the unoxidized and oxidized human αC domain dimer using enhanced sampling methods and performed free energy calculations on the most stable unoxidized conformations to determine if Met^{476} oxidation is destabilizing. A single molecular dynamics (MD) simulation isn't capable of generating a canonical ensemble on reasonable timescales. Therefore, we utilized enhanced sampling techniques, which rely on multiple simulations at different temperatures, to generate the canonical ensemble (Earl & Deem, 2005; Patriksson & van der Spoel, 2008). These methods allow us to estimate the energetic consequences of oxidation and challenge our hypothesis.

2 Materials and Methods

2.1 Initial conformations

The coordinates for the NMR solution structure of bovine αC domain with (PDB ID: 2JOR Burton *et al.*, 2007) were used to start simulations of the bovine sequence. Simulations with the human αC domain were started from a previously unpublished homology model based on PDB ID: 2JOR. The initial conformation for the simulations of the oxidized structure was obtained by replacing Met^{476} with Met(O) per analogy and subsequently performing 100 steps of steepest descent minimization with the program CHARMM (Brooks *et al.*, 2009) *in vacuo* while holding fixed all atoms except the mutated residue. While it is possible that methionine oxidation could result with methionine sulfone, with two oxygen atoms bonded to the sulfur, this is unlikely given that mass spectrometry data suggests that only the sulfoxide form is present at detectable levels (Weigandt *et al.*, 2012).

2.2 General setup of the system

The MD simulations were performed with the program NAMD (Kalé *et al.*, 1999) using the CHARMM36 force field (Brooks *et al.*, 2009) with the TIP3P model of water. The force field parameters for Met(O) were downloaded from the SwissSidechain website (Gfeller, Michielin, & Zoete, 2013) and adapted per analogy for the CHARMM36 force field. For explicit simulations of the monomer, human and bovine αC domains were inserted into a cubic water box with side lengths 75 Å resulting in a system with a total of ca. 39,000 atoms. Chloride and sodium ions were added to neutralize the system and approximate a salt concentration of 150 mM. The water molecules overlapping with the protein or the ions were removed if the distances between the water oxygen and any other atom was smaller than 3.1 Å. To avoid finite size effects, periodic boundary conditions were applied. After solvation, the system underwent 500 steps of minimization while the coordinates of the heavy atoms of the protein were held fixed and followed by 500 steps with no restraints. Each simulation was started with different initial random velocities to ensure that different trajectories were sampled despite using the same initial conformation. Electrostatic interactions were calculated within a cutoff of 10 Å while long-range electrostatic effects were taken into accounts by the particle mesh Ewald summation method (Darden, York, & Pedersen, 1993). Van der Waals interactions were treated with the use of a switch function starting at 8 Å and turning off at 10 Å. Non-bonded interactions were calculated within a cutoff of 12 Å. The dynamics were integrated with time step of 2 fs. The covalent bonds involving hydrogens were rigidly constrained by means of the SHAKE algorithm with a tolerance of 10^{-8}. Snapshots were saved every 10 ps for trajectory analysis. The Generalized Born with Solvent Accessibility (GBSA) implicit solvation method (Onufriev, Bashford, & Case, 2000) was used for T-REMD simulations. For implicit solvent simulations, electrostatic interactions cutoff was extended to 12 Å, van der Waals interactions were treated with the use of a switch function starting at 10 Å and turning off at 12 Å and non-bonded interactions were calculated within 14 Å.

2.3 Equilibration and sampling of the native states

Before production runs, harmonic constraints were applied to the positions of all heavy atoms of the protein to equilibrate the system at 300 K for a total duration of 0.2 ns. To equilibrate the position of atoms around a methionine sulfoxide side chain, harmonic constraints were kept on all heavy atoms except those of the methionine sulfoxide residue and the neighboring amino acids, and equilibration was continued for another 2 ns. After this equilibration step, the harmonic constraints were released.

In order to analyze changes in the native state of the αC domain upon oxidation, simulations were performed for a total of 20 ns each where no external forces were applied. The first 10 ns of unconstrained simulation were also considered part of the equilibration and were thus not used for analysis. During the equilibration and in all runs except T-REMD, the temperature was kept constant at 300 K by using the Langevin thermostat (Schneider & Stoll, 1978) with a damping coefficient of 1 ps^{-1}, while the pressure was held constant at 1 atm by applying a pressure piston (Feller, Zhang, Pastor, & Brooks, 1995).

2.4 Hydrogen bond analysis

In order to determine the stability of the hairpin in implicit solvent, the occupancy of each predicted backbone H-bond was calculated. H-bonds were said to be formed if the HN to O distance was less than 2.7 Å and the N-HN-O angle is at least 120°. H-bonds present in at least 60% of the simulation time are defined as stable.

2.5 Native side chain contacts

To determine if Met^{476} interacts across the dimer interface, we identified all of Met^{476} native side chain contacts. A native side chain contact is defined to occur when the distance between the centers of mass of the two side chains is not larger than 6 Å. Contacts present in at least 60% of the simulations of at least one simulation are defined as native.

2.6 Nuclear overhauser effects constraints

The MD trajectories were compared with NOE derived distance constraints. A NOE distance constraint was considered violated in the simulations if the equation

$$r_{\text{min}}^{\text{exp}} \leq \langle r(t)^{-6} \rangle^{-\frac{1}{6}} \leq r_{\text{max}}^{\text{exp}} + 0.5 \text{ Å} \tag{1}$$

was not fulfilled, where $r(t)$ is the interproton distance, in Å, at simulation time t, $r_{\text{min}}^{\text{exp}}$ is the experimentally determined lower distance limit, $r_{\text{max}}^{\text{exp}}$ is the experimentally determined upper distance limit, and $\langle\,\rangle$ represents a time average. A 0.5 Å buffer term is added to account for edge cases while introducing a minimal amount of uncertainty. NOE violations are reported as percentages, which are defined by the equation

$$NOE_{\%} = \frac{N_{\text{violations}}}{N_{r^{\text{exp}}}} \times 100\% \tag{2}$$

where $N_{violations}$ is the number of NOE violations and $N_{r^{exp}}$ is the number of experimentally determined distance ranges.

2.7 Enhanced sampling of the dimer conformations

2.7.1 Temperature replica exchange molecular dynamics simulations

Temperature replica exchange molecular dynamics (T-REMD) utilizes temperature to overcome free energy barriers (Earl & Deem, 2005). The GBSA implicit solvation model was used to decrease the number of atoms, which requires fewer replicas (Onufriev *et al.*, 2000). Eight replicas were chosen to achieve a theoretical swapping efficiency of 0.45 given the number of atoms and lower temperature of 300.0 K (Patriksson & van der Spoel, 2008). The replicas correspond to 300.0 K, 306.30 K, 312.74 K, 319.31 K, 326.02 K, 332.87 K, 339.86 K, 347.00 K, which had a mean exchange ratio of 0.43 ± 0.04 for the unoxidized simulations and 0.40 ± 0.01 for the oxidized simulations. After every 10 picoseconds, the temperature swaps are subject to the Metropolis criterion to generate a canonical ensemble. To enhance sampling, constraints on the RMSD of each hairpin were added as well as a constraint on the distance between centers of mass of the monomers. This is justified because we do not expect the hairpins to significantly change conformation upon dimerization. A short simulation in implicit solvent was performed using an initial conformation made of two vertically stacked αC monomers. A metastable conformation was found to have H-bonds formed between the monomers and this was used as the initial conformation for the production T-REMD runs. Eight replicas performed for 125 ns of simulation for 1 μs of sampling for both unoxidized and oxidized configurations.

2.7.2 Construction of the free energy landscape

An FEL was generated by calculating the radius of gyration (R_g) for each monomer of each frame. The FEL is a 2D histogram with bin widths of 0.25 Å represented as a matrix where the x- and y-axes correspond to the R_g for both monomers and the z-axis is the energy of the bin derived using the Boltzmann distribution as shown in Equation (3) where G_{Bin} is the Gibbs free energy of the bin, R is the ideal gas constant in (kcal g^{-1} mol^{-1} K^{-1}), T = 300 K and $N_{FramesInBin}$ is the number of frames in the bin.

$$G_{Bin} = RT \ln(N_{FramesInBin}) \tag{3}$$

2.7.3 Minima selection

The deepest minima were selected by selecting the minima whose Boltzmann factor relative to the deepest well is ≤ 0.2 at 300.0 K. The seven deepest local minima from the unoxidized simulation, were selected from 38 total local minima using MATLAB's "imregionalmin" function (Thompson & Shure, 2017). In the oxidized case, there were four local minima out of 48 total local minima with two of the minima being separated by a single bin. Hierarchical clustering was performed on all frames (Kelley, Gardner, & Sutcliffe, 1996) in the deepest bin in each minima to identify the representative frames.

2.8 Solvent exposure cutoff determination

Full exposure of Met^{476} occurs around 176 Å, which was determined by averaging the solvent accessible surface area (SASA) values of Met in a Ala-Met-Asp tripeptide for 1 ns in explicit solvent. Partial exposure, 88 Å, is defined as the mean SASA value between full exposure and no exposure.

3 Results

3.1 Flexibility of monomers: bovine and human

The NMR solution structure coordinates were used to build a human homology model. To justify using the homology model, we must compare the flexibility of both bovine and human sequences. As shown in Figure 2a, the bovine and human structures have very similar RMSF values between residue pairs. Notably, the bovine pseudohairpin is more flexible than the human sequence, although there aren't significant differences between bovine and human sequence flexibilities. Furthermore, there are no significant differences between the human sequence in explicit vs. implicit

3.2 Comparison of explicit vs. implicit solvent models with human αC domain

The only experimental coordinates of the αC domain are derived from an NMR solution structure of the bovine sequence. However, we are interested in using a human homology model in implicit solvent. First, we simulated the bovine sequence and human homology model each in explicit solvent. We then simulated the human

homology model in GBSA implicit solvent (Onufriev *et al.*, 2000) in preparation for T-REMD and compared the stabilities of the H-bonds that define the N-terminal hairpin to the explicit solvent simulations and the NMR data. The H-bond stabilities are reported for the bovine sequence in explicit solvent, the human sequence in explicit solvent and the human sequence in GBSA implicit solvent as shown in Figure 3b. The H-bond nearest the disulfide, 444O:464HN, is weakest in bovine and human structures, including in implicit solvent. This is due to the increased flexibility near the N-terminus as shown in Figure 2a. With the human sequence in explicit solvent, the hairpin is almost entirely formed. Introduction of implicit solvent does not alter the RMSD compared to the explicit solvent, although the hydrogen bond stabilities are slightly weaker as shown in Figure 3b. In particular, only two H-bonds are not considered stable in the implicit solvent. Neither the RMSD nor RMSF values can account for these differences, suggesting that the implicit solvent model may weaken certain H-bonds, although the effect is small. While the hairpin and pseudohairpin exhibit lower RMSD values, as seen in Figure 2b, the mean RMSD for the whole αC domain and linker region are very high, while the hairpin RMSD values are small. This illustrates the hinge-like behavior of the flexible linker region. The hairpin and pseudohairpin can move independently about the 11 residue linker, which is consistent with previous MD studies of the monomer (Burney *et al.*, 2014). Given that the GBSA implicit solvent model will not substantially alter the dynamics of the αC domain, we are justified in using it for our T-REMD simulations to improve sampling and runtime efficiency.

3.3 Comparing free energy landscapes of unoxidized and oxidized dimers

To understand the conformational heterogeneity of the αC domain, we performed T-REMD on the unoxidized and oxidized dimer configurations. By describing the FELs using the R_g of the monomers, we were able to identify local minima with reduced conformational heterogeneity. The FEL for the unoxidized dimer is shown in Figure 4a, which indicates several stable binding modes, with the deepest seven wells labeled in increasing order of depth. In addition, the FEL exhibits weak symmetry, which is expected since both monomers are chemically identical. In contrast, the FEL for the oxidized dimer is shown in Figure 4b, which shows only four deep minima and a generally flat, shallow energy surface at higher R_g values. Two degenerate states, labeled 3 and 4 in Figure 4b, are separated by a single bin. Their representative frames have an RMSD = 2.0 Å and the depth of the wells differ by 0.3 kcal. Figure 4b also displays significant symmetry along $R_{g\ 1} = R_{g\ 2}$, indicating a dearth of stable

conformations to sample upon oxidation. Both T-REMD simulations contain the same number of frames and yet the energy distributions have a difference between mean energies of $\Delta\Delta G_{mean} = 4.33$ kcal/mol due to the increased sampling of higher R_g values after oxidation.

Based on our hypothesis, we predicted that there would be a correlation between the solvent exposure of Met^{476} and high $\Delta\Delta G$ values. Figure 5 details the SASA of Met^{476} residues in each local minimum. All but one minimum has at least one Met^{476} residue that is partially exposed. The mean free energy change due to oxidation was estimated by comparing the magnitudes of the minima in each case, as shown in Equation (4). We estimate a $\Delta\Delta G_{FEL} = 6.23$ kcal/mol assuming that the energies of the unfolded states of both species are virtually identical ($G_{U\ monomer} \approx G_{O\ monomer}$). N_i is the number of frames in the ith minimum.

$$\begin{aligned} G_{O\ dimer} &= RT\ \ln(\sum_{i=1}^{4} N_i) \\ G_{U\ dimer} &= RT\ \ln(\sum_{i=1}^{7} N_i) \\ \Delta\Delta G_{FEL} &= (G_{O\ dimer} - G_{O\ monomer}) - (G_{U\ dimer} - G_{U\ monomer}) \\ &= 6.23 \text{ kcal/mol} \end{aligned} \tag{4}$$

3.4 Identifying residues at the dimer interface

The unoxidized T-REMD simulation provided a large dataset to determine which residues are commonly found at the interface. The occupancy of each residue at the interface is shown in Figure 9. Met^{476} is found at the interface in all 8 replicas, which suggests Met^{476} forms a hydrophobic core in the dimer. Residues found at the ends of the hairpin or pseudohairpin are not found at the interface very often, while residues in the hairpin and pseudohairpin are found at the interface.

4 Discussion

When fibrinogen is converted into fibrin, it stabilizes platelets to form a clot upon vascular injury. HOCl produced by neutrophil myeloperoxidase oxidizes Met^{476} and changes the porosity and diffusion constant of the clot, inhibiting fibrinolysis, leading to thrombosis. However, the exact mechanism by which oxidation structurally affects fibrin function has not been elucidated (Weisel & Litivinov, 2013). The only

structural data available about the αC domain is an NMR solution structure derived from the bovine sequence that lacks an oxidizable methionine, which hindered previous attempts to understand the mechanism (Burton *et al.*, 2007; Burton *et al.*, 2006). Previous studies predicted that the polymerization would be analogous to amyloid fibril formation via β-sheet stacking, although there has been no direct experimental evidence to support this hypothesis (Tsurupa *et al.*, 2015).

HOCl-mediated oxidation converts Met^{476} from a hydrophobic residue to a H-bond acceptor, resulting in a free energy change. The β-hairpin and pseudohairpin contain the two patches of hydrophobic residues in the domain. Met^{476} lies in the pseudohairpin, which contains the majority of the hydrophobic residues in the αC domain. By converting Met^{476} to Met(O), the hydrophobic core necessary to form dimers is interrupted by a $Met(O)^{476}$, which leads to lowered affinity between monomers per the hydrophobic effect. This contributes to the increased R_g and disorder reported in dimers, here, and in monomers, by Burney *et al.*, 2014. Our data suggest that $\Delta\Delta G_{FEL} = 6.23$ kcal/mol as a result of this post-translational modification. Both ΔΔG values are consistent order of magnitude and are positive, indicating an unfavorable energetic cost of oxidation. $\Delta\Delta G_{mean}$ being 4.33 kcal/mol illustrates a global consequence of oxidation that is also consistent in order of magnitude with our ΔΔG estimate. Furthermore, Met^{476} is found at the interface and plays a role in the dimerization process and that oxidation increases the disorder of each monomer. Explicit solvent simulations of the representative frames from each minimum suggest that the buried interfaces have consistent, yet small, surface areas, as shown in Figure 7b. This suggests that not only may oxidation affect dimerization, but it may be involved in effectively denaturing the αC domain demonstrated by an increase in R_g. Our studies suggest that Met^{476} is necessary for binding. Binding energies between αC domains has been calculated by sedimentation to be between -4.0 kcal/mol and -6.7 kcal/mol per bound monomer depending on the length of the fragments (Tsurupa *et al.*, 2009). These values are comparable to our estimates of free energy change upon oxidation, meaning that oxidation may cooperatively abrogate binding.

In conclusion, the present study highlights that αC domain dimer formation is heavily dependent on Met^{476} oxidation state. Here, we describe a method to sample dimer conformations of polypeptides using enhanced sampling and estimate free energy changes based on the most populated wells. Furthermore, we demonstrate that this method can be repeated after post-translational modifications for comparison to a wild-type. Using this method, we show that oxidation is unfavorable to αC domain dimerization. Next, we plan to challenge our method and model by identifying residues at the interface, such as Leu^{478} and others not found at the interface, such

as Thr^{486} as shown in Figure 9. By making mutations at these positions and observing the oligomeric state by size-exclusion chromatography with multi-angle light scattering (SEC-MALS) or native gel western blot, we will investigate the accuracy of our model. This model is consistent with the current understanding of fibrin fiber formation, dysfunction, and thrombosis (Davenport *et al.*, 2011; Esmon *et al.*, 2011; Weigandt *et al.*, 2012; Weisel & Litivinov, 2013; Weisel & Medved, 2001). Since we have demonstrated a mechanistic link between Met^{476} oxidation and pathological clot morphologies, clinicians with chronically inflamed or trauma patients may be able to use oxidation product biomarkers to anticipate thrombotic disease or a bleeding disorder (Selmeci *et al.*, 2006).

References

Brooks, B., Brooks, C. I., Mackerell, A. J., Nilsson, L., Petreela, R., Roux, B., *et al.* (2009). Charmm: The biomolecular simulation program. *J Comp Chem*, *30*(10), 1545–1614. doi:10.1002/jcc.21287

Burney, P., White, N., & Pfaendtner, J. (2014). Structural effects of methionine oxidation on isolated subdomains of human fibrin d and αc regions. *PLoS ONE*, *9*(1), e86981. doi:10.1371/journal.pone.0086981

Burton, R., Tsurupa, G., Hantgan, R., Tjandra, N., & Medved, L. (2007). Nmr solution structure, stability and interaction of the recombinant bovine fibrinogen alphac-domain fragment. *Biochem*, *46*(29), 8550–8560. doi:10.1021/bi700606v

Burton, R., Tsurupa, G., Medved, L., & Tjandra, N. (2006). Identification of an ordered compact structure within the recombinant bovine fibrinogen αc-domain fragment by nmr. *Biochem*, *45*(7), 2257–2266. doi:10.1021/bi052380c

Collet, J., Moen, J., Veklich, Y., Gorkun, O., Lord, S., Montalescot, G., & Weisel, J. (2005). The αc domains of fibrinogen affect the structure of the fibrin clot, its physical properties, and its susceptibility to fibrinolysis. *Blood*, *106*(12), 3824–3830. doi:10.1182/blood-2005-05-2150

Darden, T., York, D., & Pedersen, L. (1993). Particle mesh ewald - an n.log(n) method for ewald sums in large systems. *J Chem Phys*, *98*, 10089–10092. doi:10.1063/1.464397

Davenport, R., Manson, J., De'Ath, H., Platton, S., Coates, A., Allard, S., ... Brohi, K. (2011). Functional definition and characterization of acute traumatic coagulopathy. *Crit Care Med*, *39*(12), 2652–2658. doi:10.1097/CCM.0b013e3182281af5

Earl, D., & Deem, M. (2005). Parallel tempering: Theory, applications and new perspectives. *Phys Chem Chem Phys*, *7*, 3910–3916. doi:10.1039/B509983H

Esmon, C., Xu, J., & Lupu, F. (2011). Innate immunity and coagulation. *J of Thromb and Haem*, *9*, 182–188. doi:10.1111/j.1538-7836.2011.04323.x

Feller, S., Zhang, Y., Pastor, R., & Brooks, B. (1995). Constant-pressure molecular-dynamics simulations - the langevin piston method. *J Chem Phys*, *103*(11), 4613–4621. doi:10.1063/1.470648

Gfeller, D., Michielin, O., & Zoete, V. (2013). Swisssidechain: A molecular and structural database of non-natural sidechains. *Nuc Acids Res*, *41*(D1), E327–E332. doi:10.1093/nar/gks991

Kalé, L., Skeel, R., Bhandakar, M., Brunner, R., Gursoy, A., & Krawetz, N. (1999). Namd2: Greater scalability for parallel molecular dynamics. *J Comp Phys*, *151*, 283–312. doi:10.1006/jcph.1999.6201

Kelley, L., Gardner, S., & Sutcliffe, M. (1996). An automated approach for clustering an ensemble of nmr-derived protein structures into conformationally related subfamilies. *Protein Eng Des Sel*, *9*(11), 1063–1065. doi:10.1093/protein/9.11.1063

Leong, L., Chernysh, I., Xu, Y., Sim, D., Nagaswami, C., de Lange, Z., ... Weisel, J. (2017). Clot stability as a determinant of effective factor viii replacement in hemophilia a. *Res Pract Thromb Haemost*, *1*(2), 231–241. doi:10.1002/rth2.12034

Lipinski, B. (2001). Pathophysiology of oxidative stress in diabetes mellitus. *J Diabetes Complications*, *15*(4), 203–210. doi:10.1016/S1056-8727(01)00143-X

Madden, T. (2003). The ncbi handbook. In J. McEntyre, J. Ostell *et al.* (Eds.), (Chap. 16: The BLAST Sequence Analysis Tool). Bethesda, MD: National Center for Biotechnology Information. Retrieved from https://www.ncbi.nlm.nih.gov/books/NBK21097/

Martinez, M., Weisel, J., & Ischiropoulos, H. (2013). Functional impact of oxidative posttranslational modifications on fibrinogen and fibrin clots. *Free Radic Biol Med*, *65*, 411–418. doi:10.1016/j.freeradbiomed.2013.06.039

Medved, L. [LV], Gorkun, O., & Privalov, P. (1983). Structural organization of c-terminal parts of fibrinogen aα-chains. *FEBS Lett. 160*, 291–295. doi:10.1016/0014-5793(83)80985-5

Onufriev, A., Bashford, D., & Case, D. (2000). Modifications of the generalized born model suitable for macromolecules. *J Phys Chem B*, *104*, 3712–3720. doi:10.1021/jp994072s

Patriksson, A., & van der Spoel, D. (2008). A temperature predictor for parallel tempering simulations. *Phys Chem Chem Phys*, *10*, 2073–2077. doi:10.1039/b716554d

Ping, L., Huang, L., Cardinali, B., Profumo, A., Gorkun, O., & Lord, S. (2011). Substitution of the human αc-region with the analogous chicken domain generates a fibrinogen with severely impaired lateral aggregation: Fibrin monomers assemble into protofibrils but protofibrils do not assemble into fibers. *Biochem*, *50*(42), 9066–9075. doi:10.1021/bi201094v

Rosen, H., Klebanoff, S., Wang, Y., Brot, N., Heinecke, J., & Fu, X. (2009). Methionine oxidation contributes to bacterial killing by the myeloperoxidase system of neutrophils. *Proc Natl Acad Sci USA. 106*(44), 18686–18691. doi:10.1073/pnas.0909464106

Schneider, T., & Stoll, E. (1978). Molecular dynamics study of a 3-dimensional one-component model for distortive phase transitions. *Phys Rev B*, *17*(3), 1302–1322. doi:10.1103/PhysRevB.17.1302

Selmeci, L., Székely, M., Soós, P., Seres, L., Klinga, N., Geiger, A., & Acsády, G. (2006). Human blood plasma advanced oxidation protein products (aopp) correlates with fibrinogen levels. *Free Radic Res*, *40*(9), 952–8. doi:10 .1080/10715760600818789

Shacter, E., Williams, J., Lim, M., & Levine, R. (1994). Differential susceptibility of plasma proteins to oxidative modification: Examination by western blot immunoassay. *Free Radic Biol Med*, *17*(5), 429–437. doi:10.1016/0891-5849(94)90169-4

Thompson, C., & Shure, L. (2017). *Image processing toolbox^{TM} reference*. The MathWorks^{TM}.

Tsurupa, G., Hantgan, R., Burton, R., Pechik, I., Tjandra, N., & L., M. (2009). Structure, stability, and interaction of the fibrin(ogen) αc-domains. *Biochem*, *48*(51), 12191–12201. doi:10.1021/bi901640e

Tsurupa, G., Pechik, I., Litvinov, R., Hantgan, R., Tjandra, N., Weisel, J., & Medved, L. (2015). On the mechanism of αc polymer formation in fibrin. *Biochem*, *51*(12), 2526–2538. doi:10.1021/bi2017848

Weigandt, K., White, N., Chung, D., Ellingson, E., Wang, Y., Fu, X., & Pozzo, D. (2012). Fibrin clot structure and mechanics associated with specific oxidation of methionine residues in fibrinogen. *Biophys. J*, *103*, 2399–2407. doi:10.1016/j.bpj.2012.10.036

Weigandt, K. [KM], White, N., Chung, D., Ellingson, E., Wang, Y., Fu, X., & Pozzo, D. (2012). Alterations in fibrin clot structure and mechanics associated with specific oxidation of methionine residues in fibrinogen. *Biophys J. 103*(11), 2399–2407. doi:10.1016/j.bpj.2012.10.036

Weisel, J., & Litivinov, R. (2013). Mechanisms of fibrin polymerization and clinical implications. *Blood*, *121*(10), 1712–1719. doi:10.1182/blood-2012-09-306639

Weisel, J., & Medved, L. (2001). The structure and function of the αc domains of fibrinogen. *Ann NY Acad Sci. 936*, 312–327.

White, N., Wang, Y., Fu, X., Cardenas, J., Martin, E., Brophy, D., ... Chung, D. (2016). Post-translational oxidative modification of fibrinogen is associated with coagulopathy after traumatic injury. *Free Radic Biol Med*, *96*, 181–189. doi:10.1016/j.freeradbiomed.2016.04.023

5 Figures

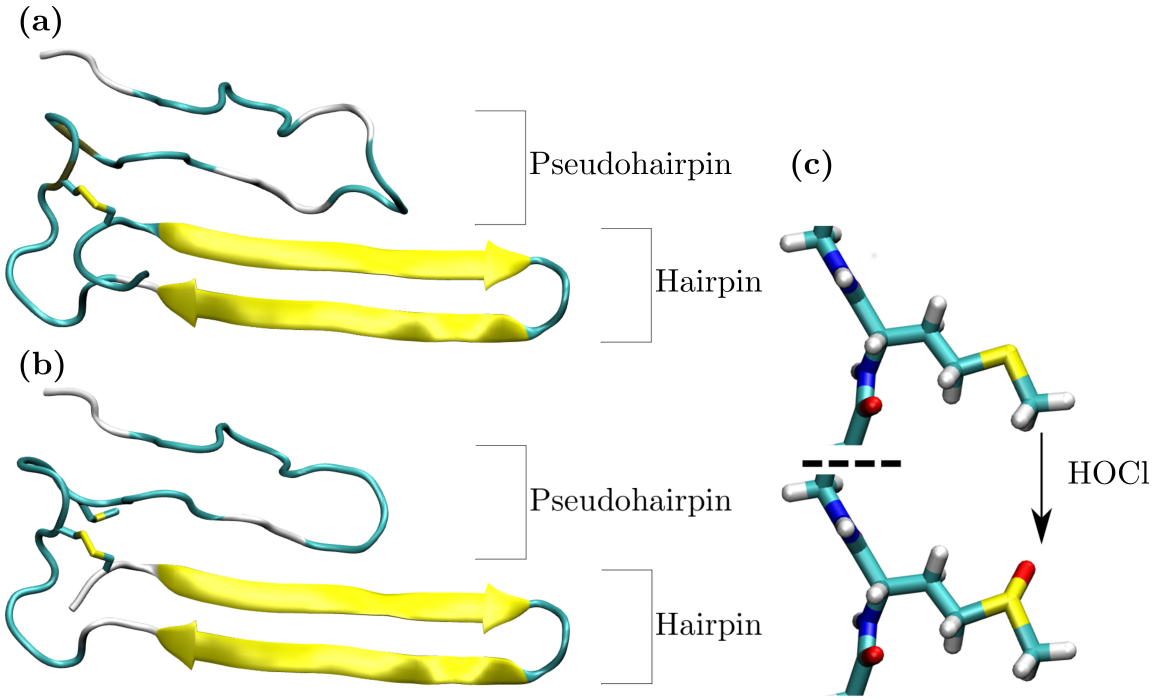

Figure 1: αC domain structures. **(a)** The bovine αC domain NMR solution structure (PDB ID: 2JOR). **(b)** The human αC domain homology model. **(c)** Conversion of methionine to methionine sulfoxide.

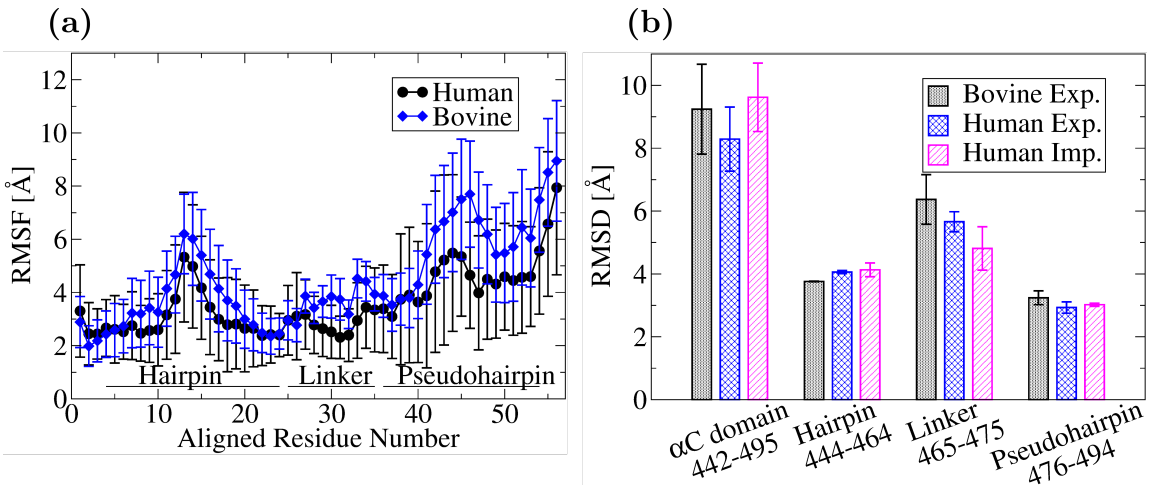

Figure 2: Comparing explicit and implicit solvation methods at room temperature. **(a)** Mean C_α RMSF calculated from the last 90 ns of the 100 ns of bovine and human simulations in explicit solvent. Averages were computed over three 300 K simulations using the same initial conformation. Error bars represent the SEM. **(b)** The C_α RMSD from the initial conformations averaged over three 300 K simulations for the last 90 ns of the 100 ns simuations. The RMSD is calculated for the αC domain without the N- and C-termini (residues 442-494), the hairpin region (residues 444-464), the linker region (residues 465-475) and the pseudohairpin region (residues 476-494). Error bars represent the SEM.

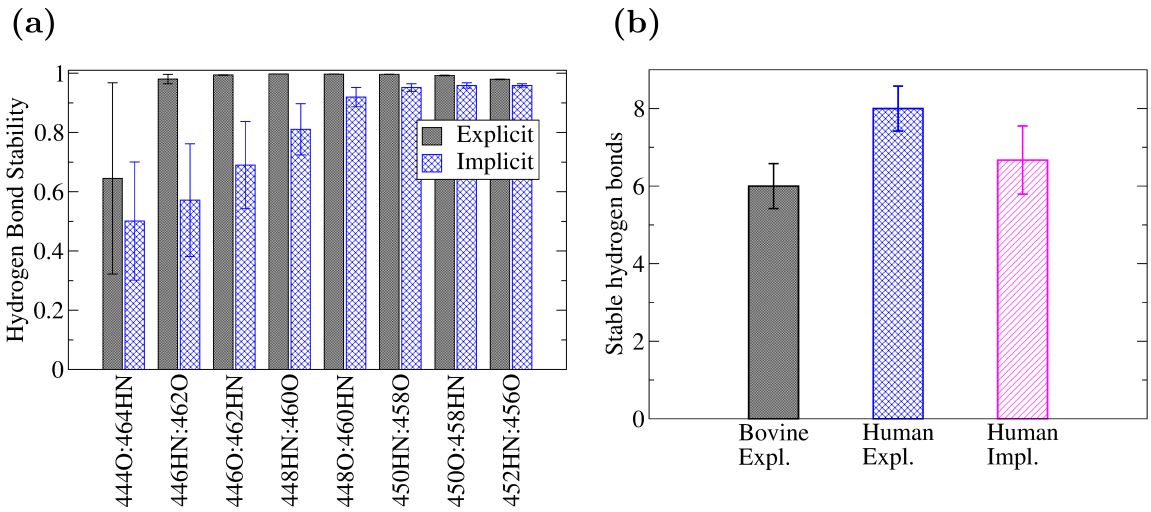

Figure 3: H-bonding **(a)** Average H-bonding stabilities were calculated for eight H-bonds along the hairpin region. Stabilities were averaged over three 300 K simulations in explicit and implicit solvents using the same initial conformation. Error bars represent the standard deviation. **(b)** The number of stable H-bonds per simulation frame were computed and averaged over three 300 K simulations using the same initial conformation. Error bars represent the SEM. The definition of a stable H-bond is given in "Materials and Methods".

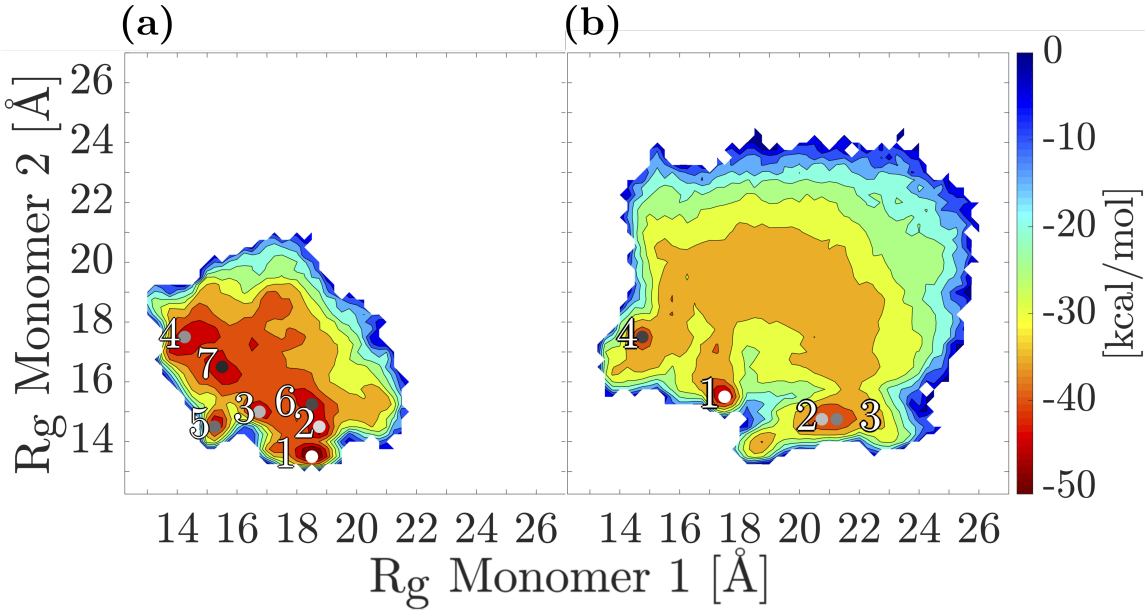

Figure 4: Free energy landscapes of fibrin αC dimers in terms of ($R_{g\,1}$,$R_{g\,2}$) space in impl icit solvent. **(a)** T-REMD simulations of the unoxidized αC domain dimer. The seven deepest minima are labeled. **(b)** T-REMD simulations of the oxidized αC domain dimer. The four deepest minima are labeled. The color bar is consistent between **(a)** and **(b)**. Dots label each minimum and are colored from white to black in decreasing order of minima depth.

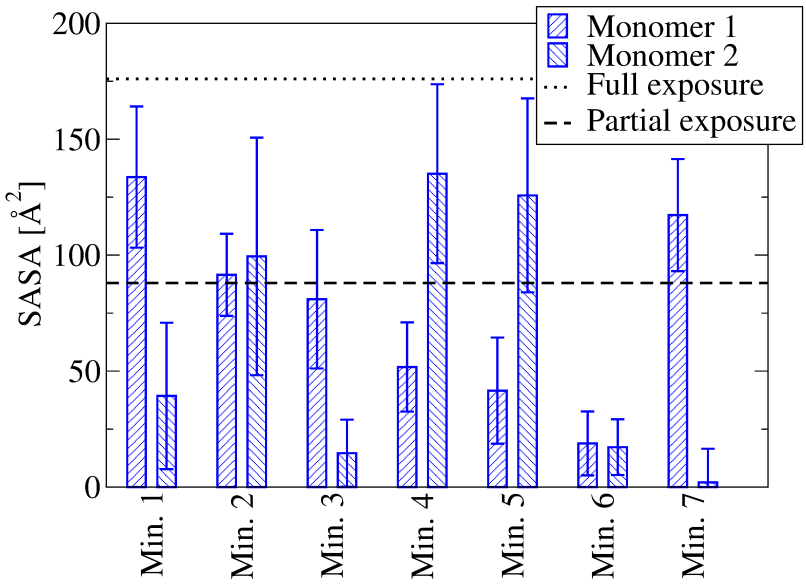

Figure 5: Solvent accessible surface area (SASA) of each Met^{476} residues in the energy minima. Average SASA for each minimum were computed over three 300 K simulations in explicit solvent. SASA values were computed from the last 40 ns of the 50 ns simulations. Error bars represent the SD. The full and partial exposure limits are labeled.

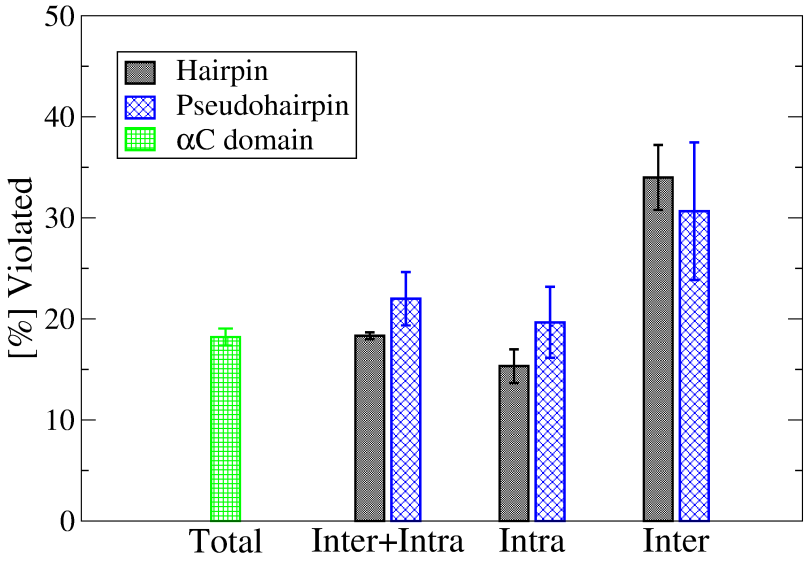

Figure 6: Percent NOE violations of the bovine sequence within and across the hairpin and pseudohairpin. Average NOE violations for explicit solvent were computed over three 300 K simulations. Violations were computed from the last 40 ns of the 50 ns simulations. Error bars represent the standard error of the mean. The total number of violations within the αC domain is reported as "total". Violations between hairpin and pseudohairpin are reported as "inter". Violations occurring within the hairpin or pseudohairpin regions are reported as "intra". The number of "Inter" and "Intra" violations for either the hairpin or pseudohairpin are reported as "Inter+Intra"

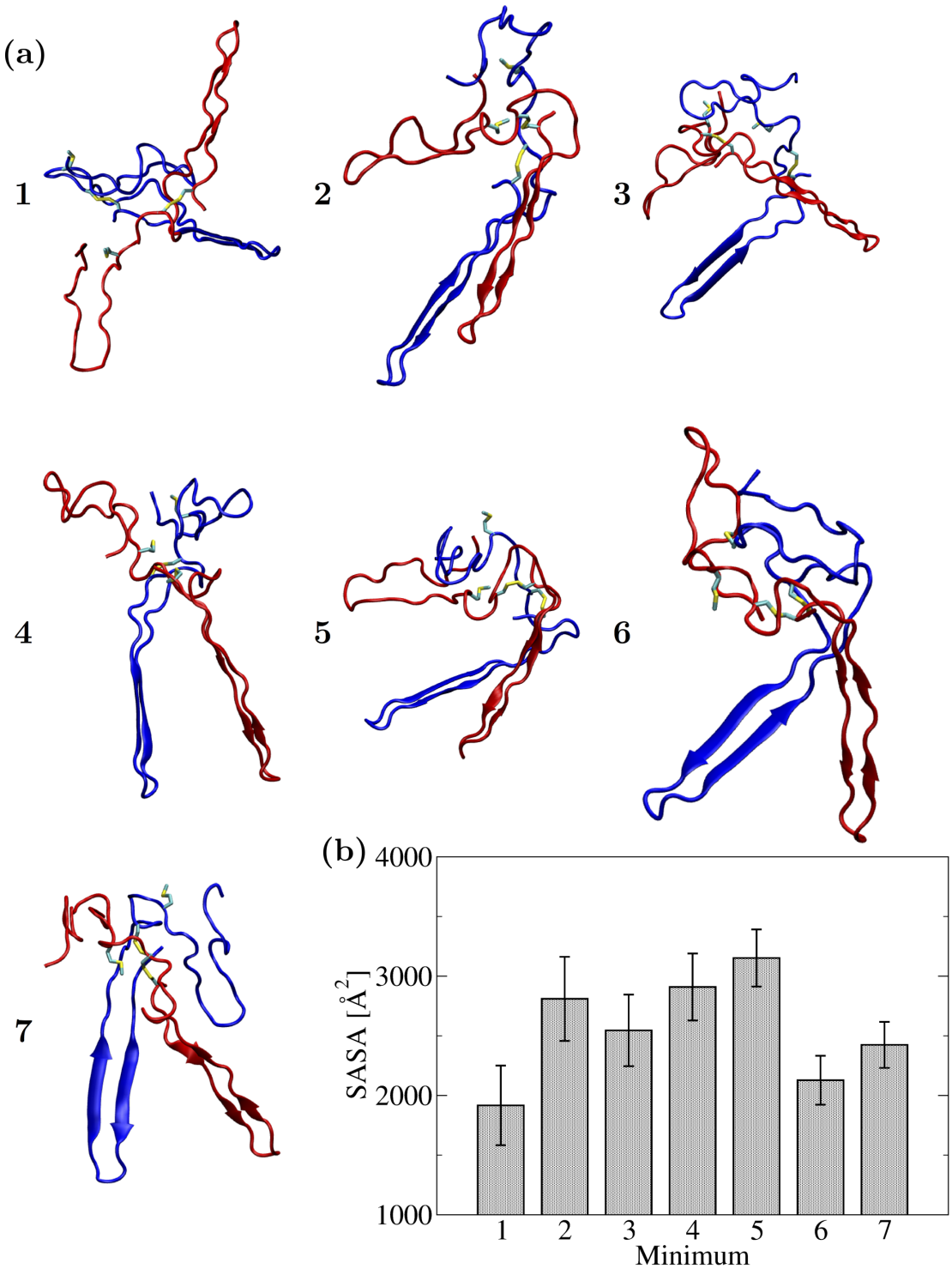

Figure 7: Representative dimer conformations from the local minima of the FEL shown in Figure 4a. Met^{476} and the disulfide Cys^{442}-Cys^{472} are represented as sticks. Monomer 1 is colored blue and monomer 2 is colored red.

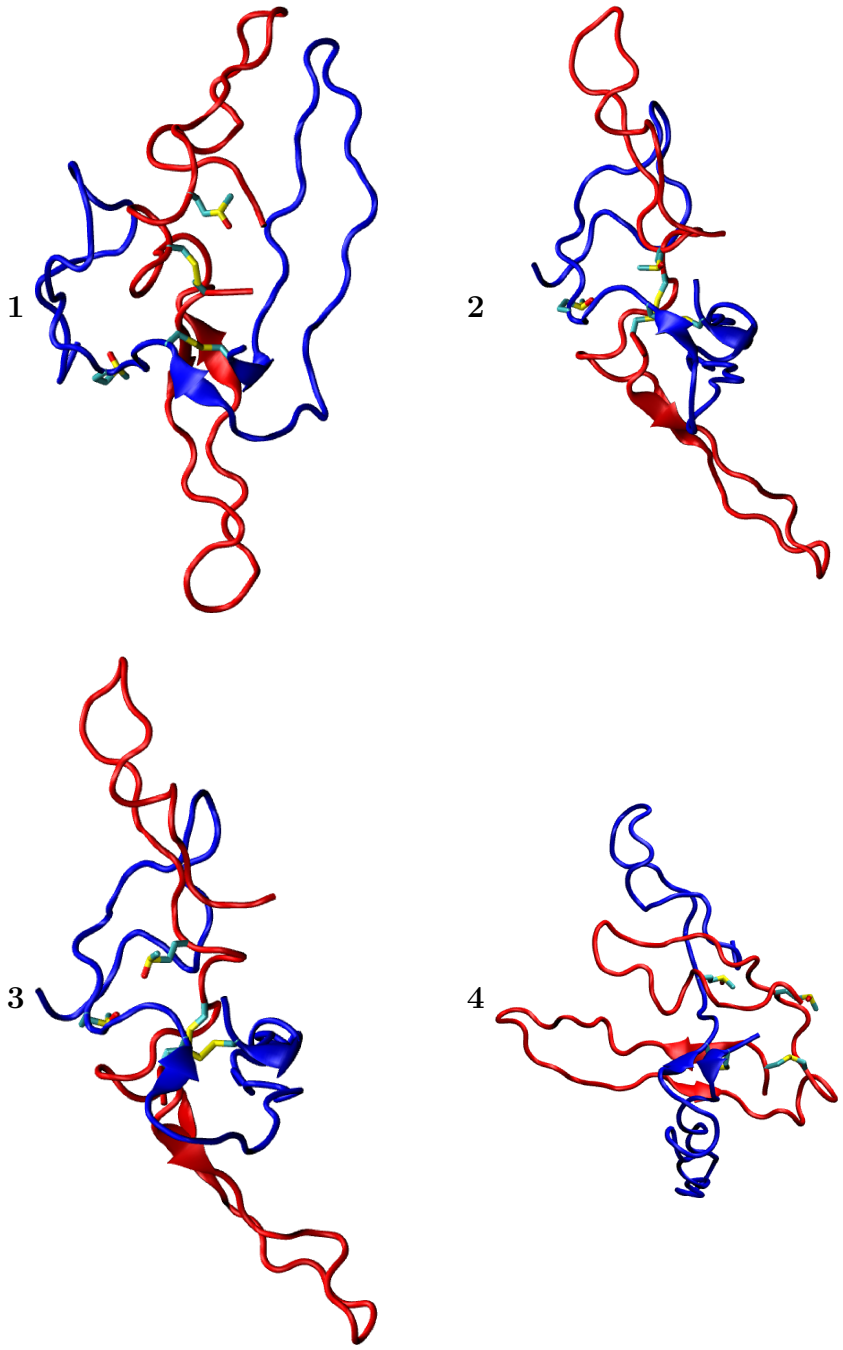

Figure 8: Representative dimer conformations from the local minima of the FEL shown in Figure 4b. Met(O)^{476} and the disulfide Cys^{442}-Cys^{472} are represented as sticks. Monomer 1 is colored blue and monomer 2 is colored red.

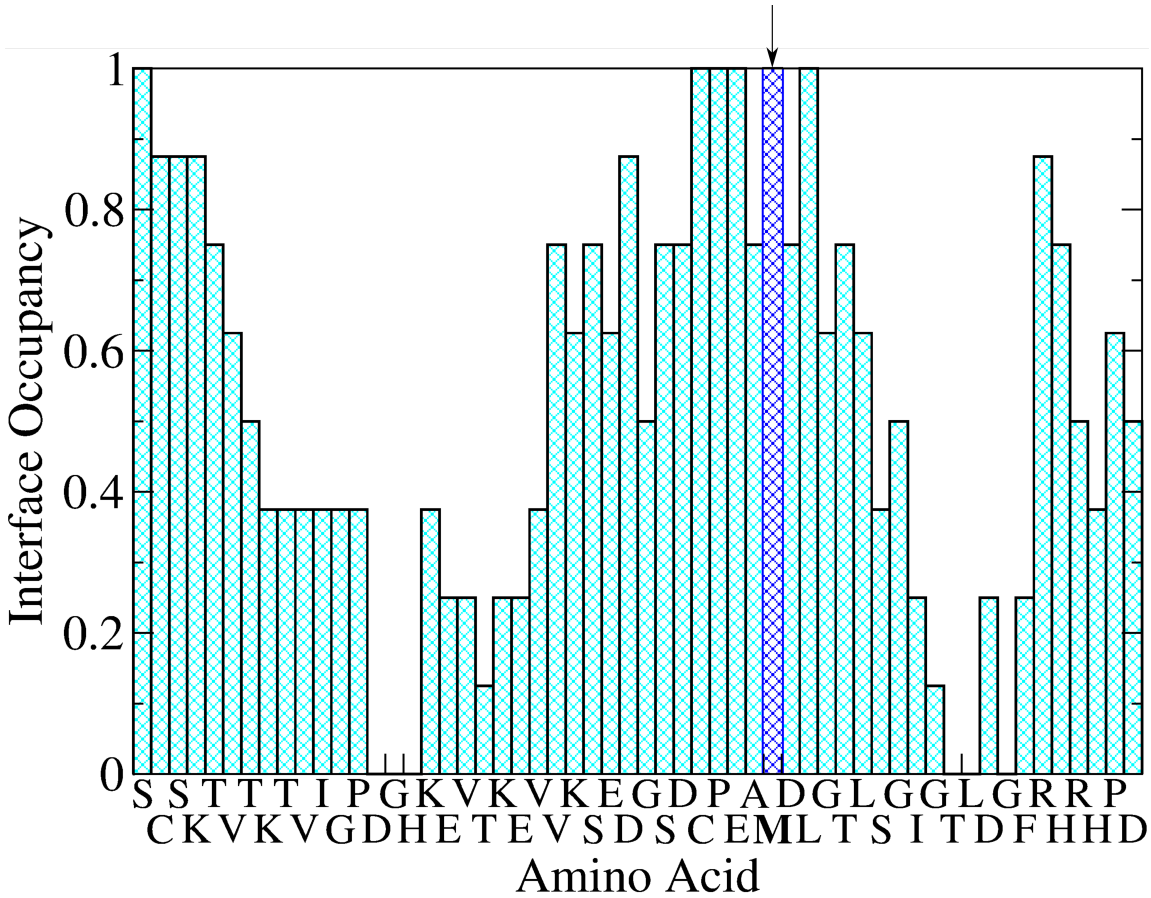

Figure 9: Interface propensity for each residue in αC domain. Occupancy is the ratio of simulation frames from all eight replicas where a native side chain contact is made. N-terminal serine is position 441.